



Supporting Online Material for

Polarization of PAR Proteins by Advective Triggering of a Pattern-Forming System

Nathan W. Goehring, Philipp Khuc Trong, Justin S. Bois, Debanjan Chowdhury, Ernesto M. Nicola, Anthony A. Hyman, Stephan W. Grill*

*To whom correspondence should be addressed. E-mail: grill@mpi-cbg.de

Published 20 October 2011 on *Science Express*
DOI: 10.1126/science.1208619

This PDF file includes:

Materials and Methods
SOM Text
Figs. S1 to S9
Tables S1 to S3
References

Other Supporting Online Material for this manuscript includes the following:

available at www.sciencemag.org/cgi/content/full/science.1208619/DC1

Movies S1 to S4

1 Material and Methods

1.1 Worm strains and growth conditions.

Worm stocks were maintained at 20-25°C and imaged at room temperature (18-22°C). Embryos were typically dissected in 0.1 M NaCl, 4% sucrose and mounted on agarose pads. For drug treatment, embryos were dissected in SGM (30) and drugs added during meiosis II prior to establishment of the eggshell permeability barrier. Transgenic worms used are described in Table S3. Some strains were provided by the *Caenorhabditis* Genetics Center (CGC) and the *C. elegans* Gene Knockout Consortium. RNAi was performed using the feeding method as described (31). *par-2*, *par-6*, and *spd-5* feeding clones were from GeneService. *mlc-4* is from (32). For the RNAi timecourse, young adults were placed synchronously on freshly made feeding plates and incubated for the indicated times. Data from embryos dissected within each time interval were pooled. Because of the syncytial nature of the *C. elegans* gonad, upon RNAi-mediated transcriptional silencing, protein is depleted gradually from the gonad cytoplasm as cytoplasm is packed into the forming oocytes. Thus, increasing duration of RNAi treatment leads to progressive depletion of the amount of target protein present in embryos undergoing polarization.

1.2 Imaging

Spinning-disk confocal images were captured on either 1) a Zeiss M3 equipped with a Yokogawa spinning disk head using a 63x/1.4 Oil PlanApochromat objective, a 488-nm argon laser (Melles Griot), an Orca ER camera (Hamamatsu) and MetaVue (Molecular Devices), or 2) an Olympus IX71 equipped with a Yokogawa spinning disk head using a 63x/1.4 Oil UPlanSApo objective, 488, 561-nm DPSS lasers, an iXon EMCCD camera and ImageIQ (Andor Technology). Exposures were typically 1 s (mCherry) or 500 ms (GFP). Most images were taken at the embryo midplane, defined as the focal plane with a maximum cross-sectional area. All domain

size measurements were taken during the stable period between the end of nuclear envelope breakdown and anaphase onset. For imaging cortical flows, images of embryos expressing a GFP fusion to the cortical myosin NMY-2 – either wild-type or *par-2(RNAi)* – were captured at the cover-slip proximal embryo surface at 1 s intervals.

1.3 Data analysis

Image analysis was performed using Fiji (<http://pacific.mpi-cbg.de>) and Matlab (Mathworks). For fluorescence profiles, a 25-pixel-wide line encompassing the membrane was extracted and computationally straightened. The profile of membrane fluorescence around the circumference of the embryo was calculated as detailed in ‘Estimating k_{on} ’ below. For examining PAR distributions over time, the center of the PAR-2 domain in each profile was defined as $x = 0$ and used for aligning individual profiles from each time point. Two half profiles from posterior to anterior, one for $x < 0$ and one for $x > 0$, were averaged to give final profiles. Each channel was then normalized to the peak fluorescence achieved during the entire timecourse. For RNAi time course experiments, profiles were smoothed using a 30-pixel averaging window, and domain size was quantified as the fraction of the profile exceeding a defined threshold above the minimum fluorescence exhibited within the profile. For analysis of *par* gene dosage and CAI altered *par-2* alleles, domains were fit using the following function:

$$I(x) = B_1 - \frac{B_2}{2} \left[\operatorname{erf} \left(\frac{\sqrt{2}}{\sigma} (x + b_L) \right) - \operatorname{erf} \left(\frac{\sqrt{2}}{\sigma} (x + b_R) \right) \right], \quad (\text{S1})$$

where B_1 , B_2 , and σ specify the displacement, magnitude, and length scale of the error function, respectively, and b_L and b_R specify the midpoint of the left and right boundaries of the domain. Domain size was calculated as

$$\text{Fractional domain size} = (b_R - b_L + 2\sigma) / \text{profile length}. \quad (\text{S2})$$

Some embryos contained two PAR-2 domains, in which case both domains were fit individually and the results added. Cytoplasmic fluorescence was measured within a region in the center of the embryo away from the membrane and avoiding the pronuclei.

To measure cortical flows, we imaged NMY-GFP at the cortex of wild-type and *par-2(RNAi)* embryos at 1 second intervals. Local velocities at each time point were obtained by particle image velocimetry (PIV), essentially as described (14). Velocities were averaged in 13 bins along the A-P axis to generate a flow profile at each time, t . The resulting 2-D patterns of flow from four embryos in each case were averaged using cytokinesis onset as a time reference. Because imaging does not capture dynamics at the poles, flow profiles we centered along x and flow velocities were set to zero at the poles. For applying spatiotemporal flow profiles to numerically investigate polarization in the model, we set flow velocities to zero for times that are outside the time window during which flows were measured. This neglects later flows that occur during cytokinesis, which likely contribute to PAR dynamics during their segregation into daughter cells as the embryo divides, but are beyond the scope of this work. We assume periodic boundary conditions in the model, and we reflected and inverted flow data across $x = 0$ before smoothing with a 2-D averaging filter and generating a 2-D interpolation function to give a full spatiotemporal flow function (Fig. S1).

1.4 Estimating model parameters and computational methods.

Simulations and numerical analysis. The *C. elegans* zygote resembles a prolate spheroid. Based on estimates from three embryos imaged by selective plane microscopy (Steffen Jaensch, MPI-CBG), we obtain a major axis $a = 27.0 \pm 1.7 \mu\text{m}$ and a minor axis $b = 14.8 \pm 1.0 \mu\text{m}$ (Mean \pm SD, n=3). Thus, we assume principle radii of $27 \times 15 \times 15 \mu\text{m}$. For the model presented here, we represent this spheroid as a finite system of length L , where L is the perimeter of an ellipse intersecting the two poles on the surface of the spheroid, and $x \in [-L/2, L/2)$.

We impose periodic boundary conditions. Note that because all perturbations are symmetric across the posterior pole, the results quantitatively agree with a similar system of length $L/2$ equivalent to a pole to pole arc of the above ellipsoid and with reflective boundary conditions $x \in [0, L/2]$. Note also that this 1-D description neglects curvature. However, calculations for a prolate spheroid geometry assuming azimuthal symmetry yields qualitatively similar results (see below).

For polarized initial states, the initial boundary position was $\pm x_0$, with $0 < x_0 < L/2$. This creates two boundaries equidistant from $x = 0$, where $x < |x_0|$ defines the posterior domain and $x > |x_0|$ defines the anterior. Within each domain, the concentration of the respective anterior or posterior PAR complex is set to its intrinsic equilibrium membrane concentration calculated without mutual antagonism, while the concentration of the opposing PAR complex is set to zero. A smooth transition was used to connect the domains across the boundaries. For homogeneous initial states, we let one or the other domain occupy the entire system. To facilitate comparisons with in vivo data, the distribution of each PAR species is normalized individually to the maximum local concentration achieved over the analyzed time period. Because of symmetry across $x = 0$, we show only half of the simulated system ($x \in [0, L/2]$).

Numerical simulations were carried out in C++, Matlab, and Python using custom software. The boundary between domains is defined as the crossing of normalized A and P concentration profiles. The boundary gradient length scale was fit as described (18) using the function

$$C(x) = B_1 + \frac{B_2}{2} \left[\operatorname{erf} \left(\frac{\sqrt{2}}{\sigma} (x - b) \right) \right], \quad (\text{S3})$$

where $C(x)$ is the concentration, b is the inflection point of the gradient, σ is the characteristic length scale of the gradient, and B_1 and B_2 scale the intensity.

Calculation of parameter space. Construction of parameter space commences by computing the real-valued homogeneous steady states P_0 and A_0 as a function of the interaction rate constants k_{PA} and k_{AP} (Figs. 2C, S2). Close to the origin of the parameter space diagram, the region in which an aPAR-dominant homogeneous state exists is limited by the line $A_0 - P_0 = 0$. Further away from the origin this line merges with the bifurcation line that borders a region of homogeneous bistability in which three real homogeneous steady state solutions exist. Two of these solutions, including one aPAR-dominated state, are homogeneously stable while the third intermediate state is homogeneously unstable. The aPAR-dominant homogeneous steady states are then examined further by performing a linear stability analysis with respect to the Fourier mode with the largest growth rate $k_1 = 2\pi/L$, thereby identifying the subregions in which this state is unstable with respect to small spatially varying perturbations. Finally, the region in which stably polarized states exist is found by means of numerical simulations along vertical lines of constant k_{PA} . Initially, for a k_{AP} value close to the suspected boundary, a suitably chosen square wave profile of aPAR and pPAR concentrations evolves to a polarized state. This state then serves as initial state for the next simulation at either increased or decreased k_{AP} . Variations of k_{AP} proceed until the amplitude, i.e. maximum concentration minus minimum concentration, of both PAR species fall below their individual thresholds and the domain state is lost. Sampling is then repeated for the next value of k_{PA} . Parameters used for the generic phase diagram in Fig. 2C and S2B are: $\rho_A = \rho_P = 1 \mu\text{m}^{-3}$, $D_A = D_P = 1 \mu\text{m}^2 \text{s}^{-1}$, $k_{\text{off},A} = k_{\text{off},P} = 1 \text{s}^{-1}$, $k_{\text{on},A} = k_{\text{on},P} = 0.3 \mu\text{m} \text{s}^{-1}$, $\alpha = \beta = 2$, $\psi = 0.3 \mu\text{m}^{-1}$ and $L = 100 \mu\text{m}$. Fig. 2B and S2A utilize parameters in Table S1.

Estimating k_{on} . In the absence of mutual antagonism, the association of PAR proteins with the membrane can be considered a process of surface adsorption, in which membrane association is governed by the adsorption rate constant, k_{on} , and the desorption rate constant, k_{off} . As a

consequence of operating in a steady state and assuming linear association rates, $k_{\text{on}}/k_{\text{off}}$ equals the ratio of the membrane surface density, ρ_s , to the cytoplasmic volumetric concentration, ρ_v . We can therefore estimate k_{on} for our system according to the following equation, where k_{on} has units of length per unit time due to the differences in dimensionality between the membrane and cytoplasmic states,

$$k_{\text{on}} = \frac{\rho_s k_{\text{off}}}{\rho_v}. \quad (\text{S4})$$

To obtain experimental estimates for k_{on} , we obtained fluorescence images from the central plane of embryos expressing either GFP::PAR-2 or GFP::PAR-6, and in which the opposing PAR complex was depleted by RNAi. This corresponds to a condition without mutual antagonism. These images were taken to reflect a thin section through the embryo 1 μm thick. We estimated ρ_v as the mean cytoplasmic fluorescence. To obtain ρ_s , a 25-pixel-wide line encompassing the membrane was extracted and computationally straightened as above. At each x along the membrane, we extracted a fluorescence profile across and perpendicular to the membrane and subtracted the mean of the local cytoplasmic and local background fluorescence (using only the cytoplasmic fluorescence did not qualitatively alter results). Based on imaging of 0.1 μm TetraSpeck beads (Invitrogen), membrane fluorescence should yield a gaussian distribution with a characteristic standard deviation $\sigma = 1.5$ pixels (0.15 μm). We therefore took fluorescence within 2σ at each x as the sum of the top six pixel values, and adjusted by a factor of 1.05 to correct for the missing fluorescence beyond 2σ . Taking intensity within 1σ (3 pixels) and adjusting by a factor of 1.5 to correct for fluorescence beyond 1σ led to similar values. Fluorescence at each x were summed over the entire circumference and normalized to length and imaging depth to give the mean surface density, ρ_s , in units of fluorescence per area. Results are in Table S1.

Estimating PAR protein concentrations. Numerical values in our model are normalized such that $\rho_P = 1 \mu\text{m}^{-3}$. An important measurement for this system is the ratio of ρ_P to ρ_A in embryos. We measured the average surface density ρ_s and the average cytoplasmic concentration ρ_v as detailed in the previous section. Applying these values to an idealized geometry of the embryo as a prolate spheroid allowed estimation of the resulting total embryo fluorescence. The resulting ratio of total PAR-6:PAR-2 fluorescence is 1.56 ± 0.2 (SD, $n = 6$). With our choice of normalization with $\rho_P = 1 \mu\text{m}^{-3}$, we therefore take $\rho_A = 1.56 \mu\text{m}^{-3}$.

An estimate of the total number of molecules was achieved by dissecting embryos expressing GFP fusions to PAR-2 and PAR-6 as the sole copies of the respective proteins and mounting them in a surrounding bath of recombinant GFP between BSA coated coverslips. Using a similar procedure to the above section, we obtained mean fluorescence data for the membrane and cytoplasm. Upon normalizing to the known concentration of the surrounding bath, we obtained estimates of the relevant densities within the embryo. Based on these data we expect stochastic fluctuations within domains on the order of $\sqrt{\Phi}$, or approximately 1%, where Φ is the mean number of molecules within a typical area explored by molecules during their lifetime of association with the membrane (Table S2). This suggests that fluctuations are quite small relative to the concentrations of molecules observed at the membrane and justifies the mean-field approach used here. Consistent with this picture, stochastic particle-based simulations yielded similar results.

Protein amounts are constant during polarity establishment. To justify the assumption of fixed pools of PAR proteins, we examined the potential role for protein production and/or degradation in polarity establishment. Protein degradation plays a role in reenforcing polarity in the 2-cell stage and beyond (33). However, there is no evidence in *C. elegans* that localized protein production or degradation is involved in the establishment of polarity within one cell

embryos. The observed depletion of cytoplasmic PAR-2 proteins during domain formation suggests pools of protein are not in excess (Fig. 4C). Finally, capturing images of polarizing embryos and estimating the total fluorescence before and after polarity establishment using a strategy similar to the section above yielded ratios (before:after) of 0.90 ± 0.11 (SD, $n=4$) for PAR-6 and 1.16 ± 0.09 (SD, $n=5$) for PAR-2, suggesting that the overall levels of PAR proteins do not change substantially during the first cell cycle.

2 SOM Text

2.1 A consideration of advection: The Péclet number.

The dimensionless Péclet number (Pe), defined as the ratio of a diffusive to an advective time scale, reflects the relative contributions of advection and diffusion to the motion of an entrained molecule. The time to traverse a characteristic distance l by diffusion with a diffusion coefficient D is given by l^2/D , while the time to traverse this distance by advective transport given a characteristic flow velocity U is l/U ; hence $Pe = Ul/D$. For $Pe \ll 1$, advection does not contribute significantly to the dynamics, whereas for $Pe \gg 1$, advection dominates. Because spontaneous detachment of PAR-6 from the membrane (with rate k_{off}) constrains the distance that molecules can be displaced, we define the characteristic distance l as the diffusive length scale $\sqrt{D/k_{\text{off}}}$ describing the typical distance a particle diffuses before spontaneous detachment from the membrane. Therefore,

$$Pe = \frac{U}{\sqrt{k_{\text{off}}D}}. \quad (\text{S5})$$

Using recent measurements of PAR protein diffusion and membrane-cytoplasmic exchange for PAR-6 ($D = 0.28 \mu\text{m}^2/\text{s}$, $k_{\text{off}} = 0.0054 \text{ s}^{-1}$) and PAR-2 ($D = 0.15 \mu\text{m}^2/\text{s}$, $k_{\text{off}} = 0.0073 \text{ s}^{-1}$) (18), together with reported characteristic cortical cytoplasmic flow rates ($U \approx 0.1 \mu\text{m}/\text{s}$) (10,

17), we obtain $Pe(\text{PAR-6}) \approx 2.5$ and $Pe(\text{PAR-2}) \approx 3.0$. Because Pe is of order unity, both advection and diffusion contribute.

To confirm the dependence of the advective trigger on Pe , we examined the effect of altering simulated flow velocities, thereby increasing or decreasing Pe . As shown in Fig. S9, alterations in Pe leads to significant defects in polarization by flows.

2.2 Physical description

For the situation with only aPAR present, the local aPAR concentration $A(x, t)$ at time t at position x at the membrane is given by Eqn. 1. We consider a finite system with periodic boundary conditions with x ranging from $-L/2$ to $L/2$, where L is the circumference of the embryo intersecting both the anterior and posterior poles. Because the total amount of aPAR appears to be constant over the polarization event (SOM 1.4), and because cytoplasmic mixing is rapid compared to events occurring on the membrane (18), A_{cyto} can be taken to be uniform in space and is calculated from the total aPAR amount minus that associated with the membrane

$$A_{\text{cyto}} = \rho_A - \psi \bar{A}; \quad \bar{A} = \frac{1}{L} \int_{-L/2}^{L/2} A dx, \quad (\text{S6})$$

where ρ_A sets the total aPAR amount and ψ is the surface to volume conversion factor, assuming a prolate spheroidal geometry for the embryo. The effects of curvature do not alter the general behavior of the 1D model presented here (SOM 2.4). To specify $v(x, t)$, cortical flows were quantified through the cell cycle in embryos depleted for PAR-2 (Fig. S1A). Specifying the initial state as the unique homogeneous steady-state solution to Eqns. 1 and S6 without flow, we solved Eqns. 1 and S6 numerically to calculate the transient displacement of aPAR in response to measured flow velocities.

For the full description with both species, P_{cyto} is analogously given by the total pPAR amount minus that associated with the membrane,

$$P_{\text{cyto}} = \rho_P - \psi \bar{P}; \quad \bar{P} = \frac{1}{L} \int_{-\frac{L}{2}}^{\frac{L}{2}} P dx, \quad (\text{S7})$$

with ρ_P setting the total pPAR amount. To specify $v(x, t)$, cortical flows were quantified through the cell cycle in wild type embryos (Fig. S1B). We selected a parameter regime that permits both a stable polarized and a stable anterior-like unpolarized state (Table S1), taking as the initial condition the stable unpolarized anterior-like state.

2.3 Bistability

For $\alpha \geq 1, \beta > 1$ or $\alpha > 1, \beta \geq 1$, Eqns. 3 permit bistability in the reaction terms. Calculation of the nullclines of Eqns. 3 ($R_A = R_P = 0$) for an appropriate set of fixed cytoplasmic concentrations A'_{cyto} and P'_{cyto} can yield two stable fixed points that correspond to anterior- and posterior-like states of the membrane (Fig. 2B). Examination of the parameter space defined by k_{AP} and k_{PA} in the absence of flow for regimes satisfying $\alpha \geq 1, \beta > 1$ or $\alpha > 1, \beta \geq 1$ reveals regions where a homogeneous anterior-like solution, a posterior-like solution, or both are possible (Fig. 2C, S2). Both anterior- and posterior-like homogeneous solutions are linearly stable with respect to small spatial perturbations over much of the region where they individually exist. Interestingly, if the system becomes unstable, the first unstable and fastest growing mode at the instability is $k_1 = 2\pi/L$, which is the one that matches system length. This an attractive property for a cell polarity system since it will tend to divide the system into two equal halves, independent of the size of the cell. A stable polarized solution, invariant with respect to translation along the x axis, also exists over a large region of parameter space. Important for our purpose here, the region that permits stable polarized solutions overlaps the regions permitting a stable homogeneous anterior-like steady state (Fig. 2C ii). In these overlap regimes, a transition from the unpolarized anterior-like state to a polarized state is possible only through application of a perturbation that exceeds a critical size. Note that the coexistence of stable

polarized solutions with *unstable* homogeneous solutions permits polarization in response to stochastic fluctuations (Fig. 2C iii). However, for the *C. elegans*-specific parameters, this region of coexistence represents only a small fraction of parameter space (Fig. S2A).

2.4 Additional model discussion

Alternate PAR interaction schemes. For the purposes of our model, we used simple mass action terms incorporating a higher order non-linear dependence of PAR-2 detachment rates on PAR-6 stoichiometry. These terms satisfy the requirement for bistability. However, a variety of specific interaction terms are compatible with this general model provided they satisfy this requirement (19, 24). As an alternative to the simple mass action scheme, we examined a negative feedback regime incorporating cooperative Hill functions such that the reactions terms are given by

$$\begin{aligned} R_A &= k_{\text{on},A} A_{\text{cyto}} - k_{\text{off},A} A - k'_{\text{AP}} A \frac{P^\alpha}{k_{\text{P}}^\alpha + P^\alpha} \\ R_P &= k_{\text{on},P} P_{\text{cyto}} - k_{\text{off},P} P - k'_{\text{PA}} P \frac{A^\beta}{k_{\text{A}}^\beta + A^\beta}, \end{aligned} \quad (\text{S8})$$

where k'_{AP} and k'_{PA} are the revised rate constants governing the antagonism and k_{A} and k_{P} are the respective Hill coefficients. For a choice of suitable parameters that ensure operation within a saturating regime, we obtain qualitatively similar results (Fig. S3). Parameters were identical to Table S1 with the following exceptions: $k'_{\text{AP}} = 0.235 \text{ s}^{-1}$, $k'_{\text{PA}} = 0.25 \text{ s}^{-1}$, $k_{\text{A}} = 0.1 \mu\text{m}^{-2}$, $k_{\text{P}} = 0.2 \mu\text{m}^{-2}$.

Examination of parameter space. Examination of the existence and stability of homogeneous and polarized solutions for a *C. elegans*-specific parameter set for the parameter space defined by k_{AP} and k_{PA} yielded the same topology as Fig. 2C, but distorted in space. We find regions where the homogeneous anterior-like state exists, where it is stable, where it is unstable,

and where it overlaps with regions permitting stable polarized solutions. Note that the region permitting unstable homogeneous solutions (Fig. S2A iii) now occupies only a narrow slice of parameter space, suggesting that such regimes are less likely than stable homogeneous solutions given the measured parameters. In particular, only a small fraction of parameter space simultaneously permits an unstable homogeneous solution, a stable polarized solution, and roughly equal-sized anterior and posterior domains as would seem to be required for a spontaneously polarizing model for the *C. elegans* embryo. This is consistent with the idea that polarization in *C. elegans* relies on dedicated cues such as flow and is not spontaneous.

We have primarily focused on the existence and stability of the homogeneous anterior-like state because this state reflects the condition of the embryo prior to polarization. The model displays similar properties with respect to the corresponding posterior-like state, including permitting both stable and unstable homogeneous steady states. The relevant regions in parameter space are similar to those for the anterior-like homogeneous state and are shown for the parameter set used in Fig. 2C for illustration purposes (Fig. S2B).

Stability to changes in aPAR:pPAR ratio. In Fig. S6, we examine the stability of polarized and unpolarized steady-states with respect to changes in total amounts of the two PAR species. We were particularly interested in the response of the stability of the polarized state to changes in relative protein amounts, since such perturbations are possible within *C. elegans* through depletion or overexpression as shown in Fig. 4. Alterations in ρ_A and ρ_P both yield changes in the positioning of the PAR boundary. Beyond a given range, a polarized steady state is not possible. Loss of polarity due to changes in one species can be typically rescued by altering either the amount (ρ) or activity ($k_{AP/PA}$) of the opposing species, consistent with in vivo experiments in which mutations in *PAR-2* can be suppressed by mutations or depletion of aPARs, e.g. (6).

Consideration of curvature. The general statement for the dynamics of aPARs and pPARs, with respective concentrations A and P on the membrane is

$$\begin{aligned}\partial_t A &= D_A \nabla^2 A - \nabla \cdot (A \mathbf{v}) + R_A \\ \partial_t P &= D_A \nabla^2 P - \nabla \cdot (P \mathbf{v}) + R_P,\end{aligned}$$

with R_A and R_P given by Eqns. 3. For a *C. elegans* embryo, the dynamics occur on a two-dimensional surface that is approximately a prolate spheroid with major axis $a = 27 \mu\text{m}$ and minor axis $b = 15 \mu\text{m}$. It is therefore natural to operate in prolate spheroidal coordinates (ν, ϕ) , where $\phi \in [0, 2\pi)$ is the azimuthal angle and $\nu \in [0, \pi]$ is the polar angle, zero at the posterior pole and π at the anterior pole. The flow and concentration profiles in the embryo are typically independent of ϕ during polarity establishment, so we assume azimuthal symmetry. As a result, $A = A(\nu)$, $P = P(\nu)$, and $\mathbf{v} = (v(\nu), 0)$. Using this assumption and the expressions for the Laplacian and divergence in prolate spheroidal coordinates,

$$\begin{aligned}\partial_t A &= \frac{D_A}{c^2(\sinh^2 \mu_0 + \sin^2 \nu)} (\partial_\nu^2 A + \cot \nu \partial_\nu A) \\ &\quad - \frac{1}{c\sqrt{\sinh^2 \mu_0 + \sin^2 \nu}} \left(\partial_\nu(Av) + \frac{\sinh^2 \mu_0 \cot \nu + \sin 2\nu}{\sinh^2 \mu_0 + \sin^2 \nu} Av \right) + R_A,\end{aligned}$$

where

$$\mu_0 = \tanh^{-1}(b/a) \quad \text{and} \quad c = a/\cosh \mu_0.$$

The governing equation for P is analogous. The average concentration of aPAR (for use in the expression for R_A) is

$$\bar{A} = \frac{c^2 \sin \alpha}{b^2 \sin \alpha + ab\alpha} \int_0^\pi d\nu A \sinh \mu_0 \sin \nu \sqrt{\sinh^2 \mu_0 + \sin^2 \nu},$$

where $\alpha = \cos^{-1}(b/a)$. The expression for \bar{P} is analogous.

The assumption of azimuthal symmetry imposes zero-velocity and zero-diffusive flux boundary conditions at the poles. Therefore, the boundary conditions are

$$\partial_\nu A(0) = \partial_\nu A(\pi) = \partial_\nu P(0) = \partial_\nu P(\pi) = v(0) = v(\pi) = 0.$$

As a consequence of these boundary conditions, all nonhomogeneous profiles of A and P reach extrema at the poles.

If we choose to neglect the contribution of curvature to the dynamics, only the diffusive and advective terms are affected.¹ Neglecting curvature in these terms gives, e.g. for aPAR,

$$\partial_t A = \left(\frac{2\pi}{L}\right)^2 D_A \partial_\nu^2 A - \frac{2\pi}{L} \partial_\nu(Av) + R_A,$$

where L is the circumference around the ellipsoid going through both poles. Making the substitution $x = L\nu/2\pi$ recovers Eqns. 2.

Strictly speaking, $x \in [0, L/2]$, and the boundary conditions are

$$\partial_x A(0) = \partial_x A(L/2) = \partial_x P(0) = \partial_x P(L/2) = v(0) = v(L/2) = 0.$$

However, it is convenient both for analytical and numerical analysis of the dynamical system to consider periodic boundary conditions. We therefore extend the domain of x to $x \in [-L/2, L/2]$ such that it includes an entire circumference around the ellipsoid running through the poles. To enforce azimuthal symmetry, A and P must be even functions of x and v must be an odd function of x , or

$$A(x) = A(-x), \quad P(x) = P(-x), \quad \text{and} \quad v(x) = -v(-x).$$

Azimuthal symmetry also dictates that

$$A(L/2 - x) = A(-L/2 + x), \quad P(L/2 - x) = P(-L/2 + x),$$

¹ \bar{A} is defined as the average concentration on the membrane and is not dependent on the curvature of the surface, though its calculation can be more complicated for curved surfaces. The other terms in R_A are obviously independent of curvature.

and

$$v(L/2 - x) = -v(-L/2 + x).$$

For both of these conditions to hold, A and P must be even periodic functions and v must be an odd periodic function, all with period L . If we start with an initial condition in which A and P exhibit this character and the imposed velocity profile does as well for all time, then A and P will remain even periodic functions of period L . This is evident when one notes that when A and P are even and v is odd, the right hand side of Eqns. 2 consists of an even function. Therefore, we can use periodic boundary conditions in our analysis without introducing error (beyond the neglect of curvature), provided we enforce that v is odd and A and P are initially even, all with period L .

To check the effect of neglecting curvature on the dynamics of the concentration profiles, we computed the temporal evolution of the concentration profiles of the PAR proteins in prolate spheroidal coordinates and compared them to those for a flat surface. The results reveal qualitatively similar behaviors (Fig. S8).

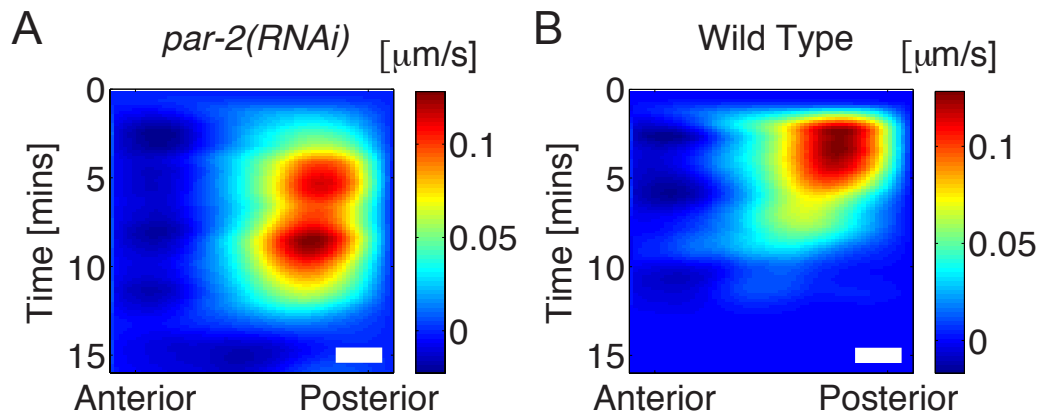


Figure S1. Spatiotemporal actomyosin cortical flow profiles. Particle image velocimetry on time-lapse images of NMY-2::GFP expressing embryos allows measurement of cortical flow velocities as a function of time and space for both (A) *par-2(RNAi)* and (B) wild-type embryos. Positive velocities reflect movement from posterior to anterior. Bars, 10 μm .

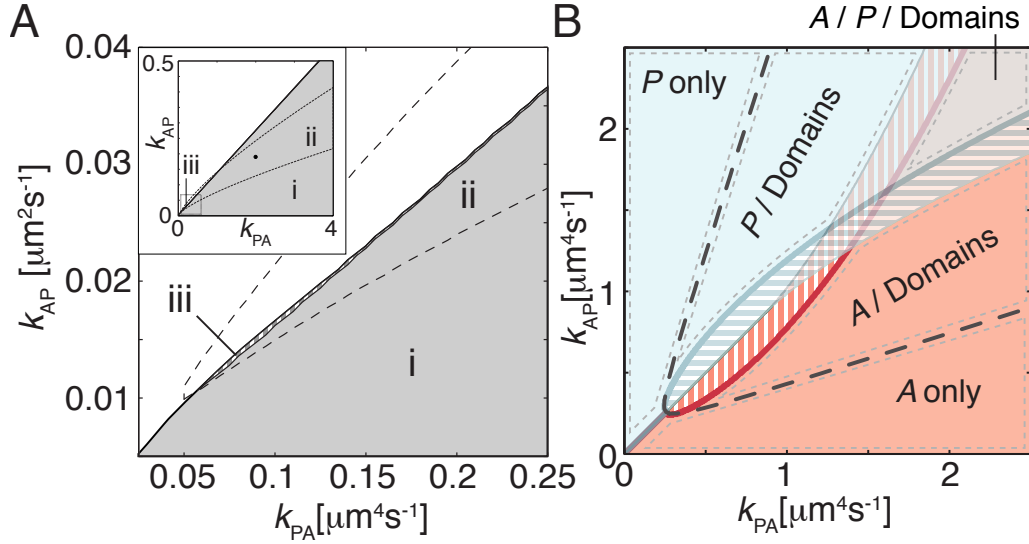


Figure S2. Additional parameter space diagrams for *C. elegans*-specific and illustrative parameter sets. (A) Regions of parameter space defined by k_{AP} and k_{PA} that permit either polarized or homogeneous anterior-like states. Similar to Fig. 2C, but for the *C. elegans*-specific parameter set. Note the distortion of the regions and the much reduced region of instability relative to the illustrative parameter set in Fig. 2C. These distortions are primarily due to asymmetry arising from the choice of $\alpha = 1$, $\beta = 2$, and the reduced values for $k_{\text{on},A}$, $k_{\text{on},P}$, and ψ relative to the illustrative parameter set. Homogeneous *A* states exist within the shaded region, where they are stable, and within the cross-hatched region, where they are unstable. The dashed line encloses the region permitting stable polarized states (encompassing regions ii, iii). In region i, the homogeneous *A* state is stable and does not coexist with a polarized solution. In region ii, both homogeneous *A* and polarized steady states exist and are stable. Here, polarization requires perturbation beyond a threshold. In region iii, both homogeneous *A* and polarized steady states exist, but the homogeneous *A* state is linearly unstable. Here, pattern formation will occur spontaneously in the presence of stochastic fluctuations. Inset shows the parameter space for an extended range of parameters, including the values for k_{AP} and k_{PA} used in the simulations (black dot). Note that the region of stable coexistence (ii) spans an increasing fraction of parameter space with increasing k_{AP} and k_{PA} . (B) Complete parameter space diagram for the illustrative parameter set in Fig. 2C, but showing the regions permitting the existence and stability of homogeneous *A* and *P* steady states. Blue regions indicated the existence of the homogeneous *P* state, while red indicates the existence of the homogeneous *A* state. Stripes denote regions where these states are unstable. The region enclosed by the dashed black line permits a stable polarized solution. Light gray dashed lines indicate regions with the indicated properties, including permitting only a single stable homogeneous steady state (*A* only, *P* only), a single stable homogeneous steady state and a stable polarized solution (*A* / Domains, *P* / Domains), or both stable homogeneous steady states and a stable polarized solution (*A* / *P* / Domains).

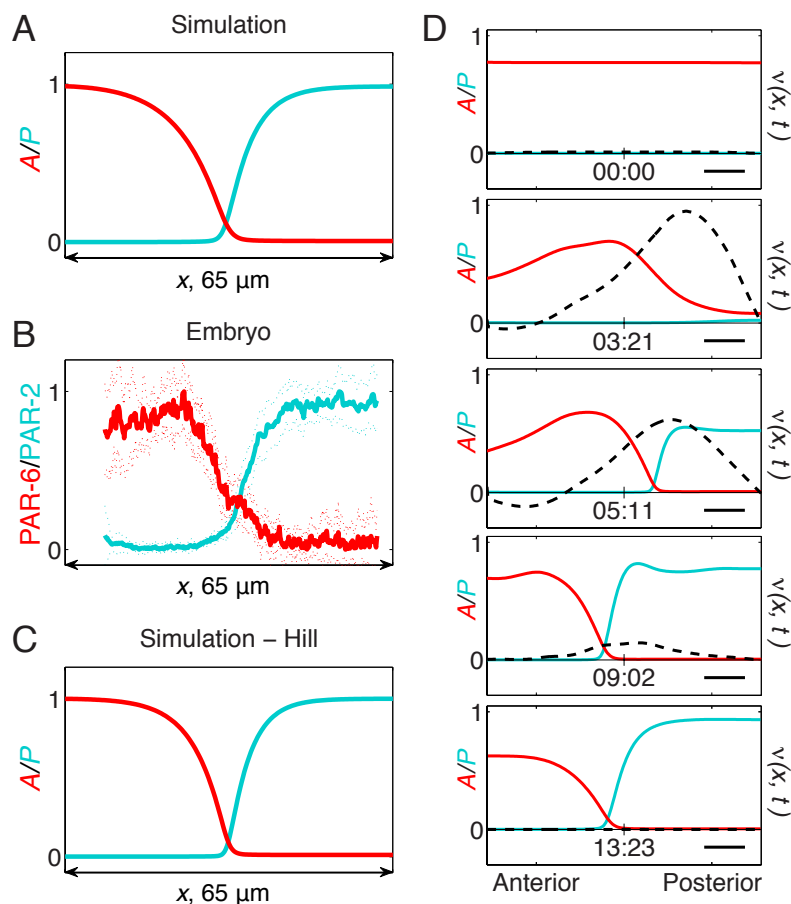


Figure S3. Reproduction of in vivo characteristics of PAR domains by a PAR reaction-diffusion model. (A) Polarized steady-state solution of the reciprocal feedback model for the parameters in Table S1. (B) Measured distributions of PAR-6 (red) and PAR-2 (cyan) during the stable domain maintenance period as reported in (18). Mean \pm SD shown ($n = 33$ anterior to posterior profiles). Note the characteristic overlapping and opposing boundary gradients are evident in both cases. Estimates of the boundary gradient length scales for each are similar (A vs. PAR-6: 12.6 vs. 10.6 μm ; P vs. PAR-2: 8.7 vs. 7.8 μm). Importantly, the PAR-6/aPAR gradient is broader, consistent with the more rapid diffusion of PAR-6 relative to PAR-2. Note we previously reported quantitation of the in vivo boundary gradients in (18) and include an updated data set here for comparison purposes. (C-D) Modified interaction terms incorporating saturation kinetics (Hill functions) yield a similar steady state (C) and spatiotemporal pattern of PAR protein distributions during advective polarization by flow (D). Bars, 10 μm .

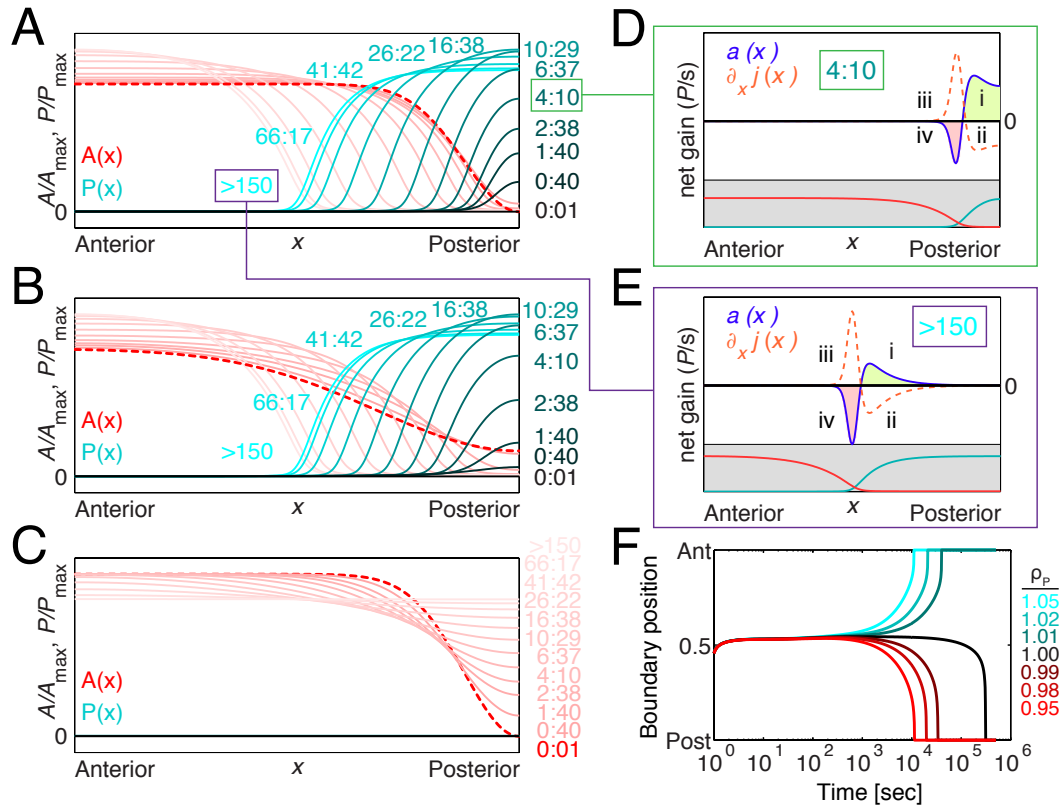


Figure S4. Stalling of domain growth in the PAR reaction-diffusion model: The no-flow regime. (A) When triggered by an instantaneous depletion of A from the posterior (dashed red line), P domain formation exhibits roughly three phases: a rapid phase in which boundary gradients acquire their characteristic shapes and length scales (0 to 10 min.), a migration phase in which the posterior domain expands at the expense of the anterior (10 to 40 min.), and finally a stalling phase in which posterior domain growth stalls (>40 min.). Time points (min:ss) are color-coded. (B) As in (A), but with a broader, but shallow perturbation. (C) As in (A-B) but applying a perturbation that fails to trigger polarization. (D-E) Plot of net gain/loss of P per unit time at the membrane due to reactions ($a(x)$, blue line) or lateral diffusion (flux divergence $\partial_x j(x)$, dashed orange line) for early (D, 4:10) and late (E, >150) time points from (A). PAR distributions (A - red, P - cyan) are shown in inset below. During domain growth (D), net gain by association posterior to the boundary (i, green region) exceeds loss by diffusive flux toward the anterior (ii). Anterior to the boundary, gain due to diffusive flux coming from the posterior (iii) exceeds losses by dissociation (iv, orange region). These imbalances drive accumulation of P in the boundary region, extending the domain. As the system approaches steady state (E), net gain/loss due to reaction are balanced everywhere by net gain/loss due to diffusive flux. (F) Substitution of non-limiting pools of both PAR species eliminates front-stalling behavior and results in a failure to stabilize the position of A-P boundary.

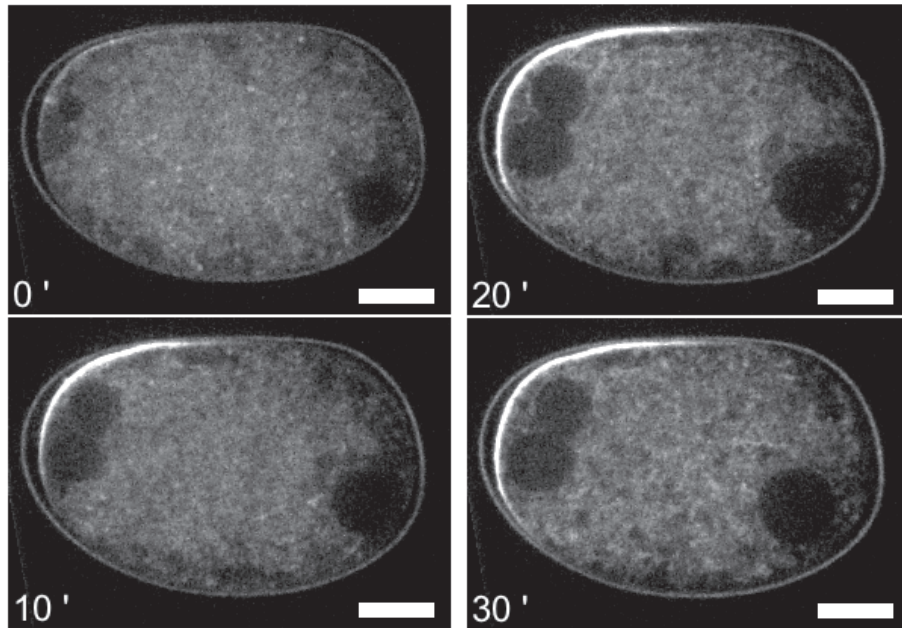


Figure S5. Polarization in a no-flow regime. A GFP::PAR-2 expressing embryo was subject to *mlc-4(RNAi)* for 30 hours and treated with nocadazole and cycloheximide during meiosis II. Nocadazole (30 $\mu\text{g}/\text{ml}$) is added to disrupt microtubule-dependent invaginations, which tend to remove PAR-2 from the cortex and can disrupt domain growth characteristics. Cycloheximide (100 $\mu\text{g}/\text{ml}$) arrests embryos prior to nuclear envelope breakdown and prevents progression through mitosis and subsequent cell cycles, which can affect PAR dynamics. This allows analysis of longer-term growth characteristics of the PAR-2 domain. Note that polarity is not initiated from the male pronucleus (right) as is seen in wild-type embryos. This is common in embryos where the normal microtubule/centrosome/flow-based signaling pathway is compromised. However, because PAR-2 defines the ‘posterior-ness’ of the embryo, we define posterior relative to the center of the PAR-2 domain for the purposes of Fig. 3F. Still images at the indicated times (min.) following appearance of an initial PAR-2 enriched patch. Note that meiotic cytokinesis failed due to a lack of MLC-4 resulting in three pronuclei. Bars, 10 μm .

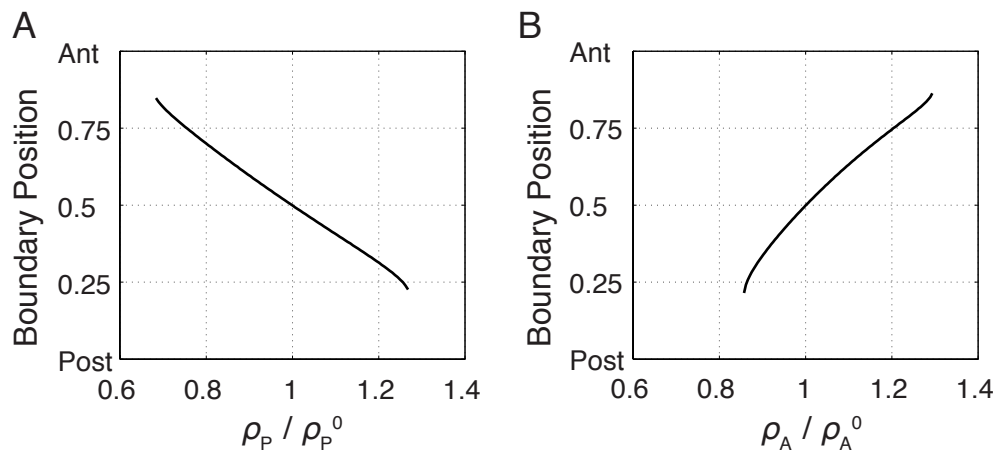


Figure S6. PAR boundary position depends on relative protein amounts. Steady-state PAR boundary position is plotted as a function of relative changes in (A) the amount of pPARs (ρ_P/ρ_P^0) or (B) the amount of aPARs (ρ_A/ρ_A^0). All other parameters were held constant at the values reported in Table S1. Values for which no curve is plotted result in an unstable polarized state.

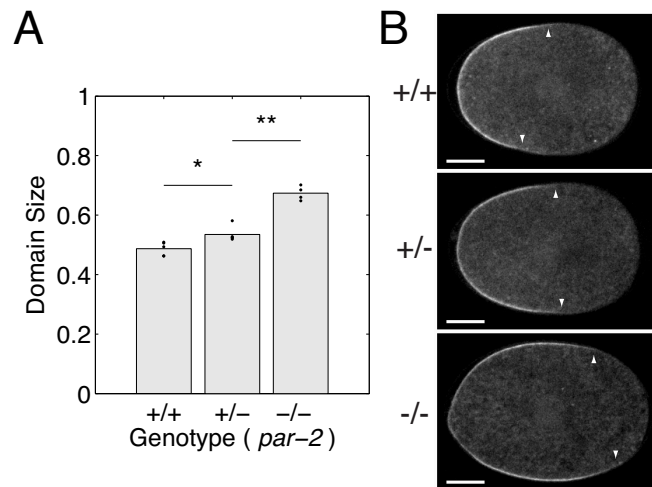


Figure S7. Anterior PAR domain size is sensitive to *par-2* gene dosage. TH417 expresses GFP-PAR-6 and is heterozygous for the *par-2* null allele *ok1723*, balanced by the sC1 balancer carrying a recessive *dpy-1* marker. Worms heterozygous for *par-2* (+/-) appear wild-type and their embryos undergo asymmetric division. Homozygous *par-2(ok1723)* mutant worms (-/-) also appear wild-type, but embryos from these adults can be easily scored since they undergo symmetric division due to a lack of functional PAR-2. Homozygous wild-type worms (+/+) are *dpy*. Examination of embryos from each class showed significant differences in the size of the PAR-6 domain ($*p < 0.05$, $**p < 0.01$, Student's t-test). Note that PAR-6 domain size is never 1.0 in -/- embryos at the measured time (nuclear envelope breakdown) due to the relatively slow spreading of PAR-6 into the posterior after flows cease.

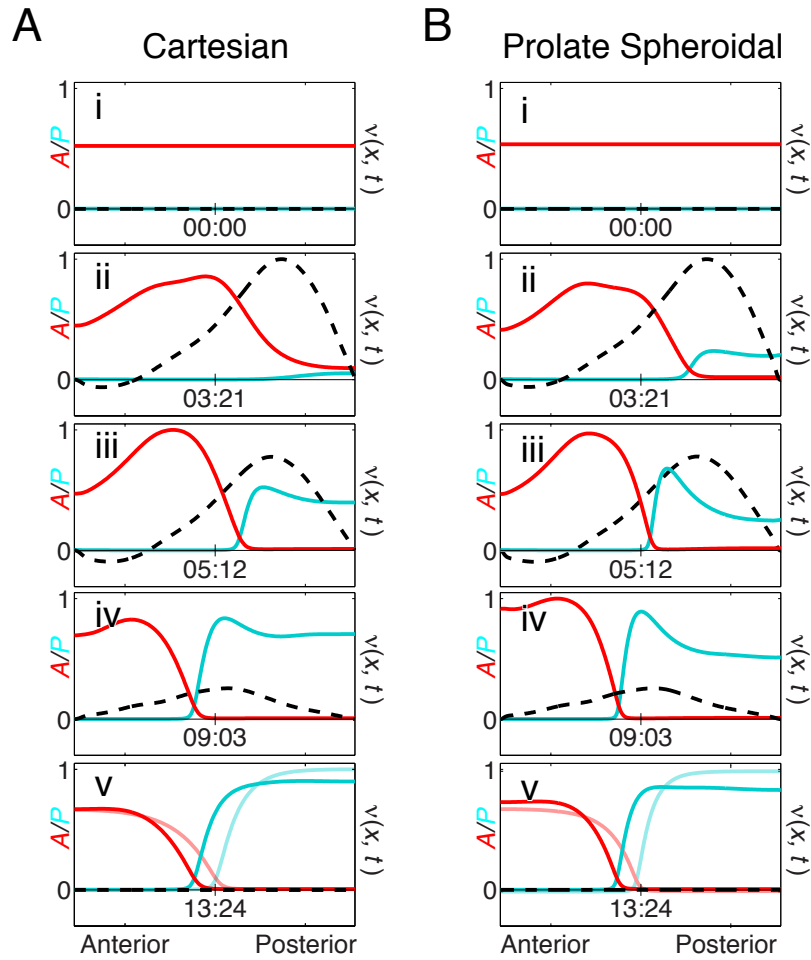


Figure S8. Effects of spheroidal geometry on polarization. A direct comparison of polarization dynamics in (A) Cartesian and (B) spheroidal coordinate systems. As in Figure 3, the shaded profiles in (v) represent the steady state profiles.

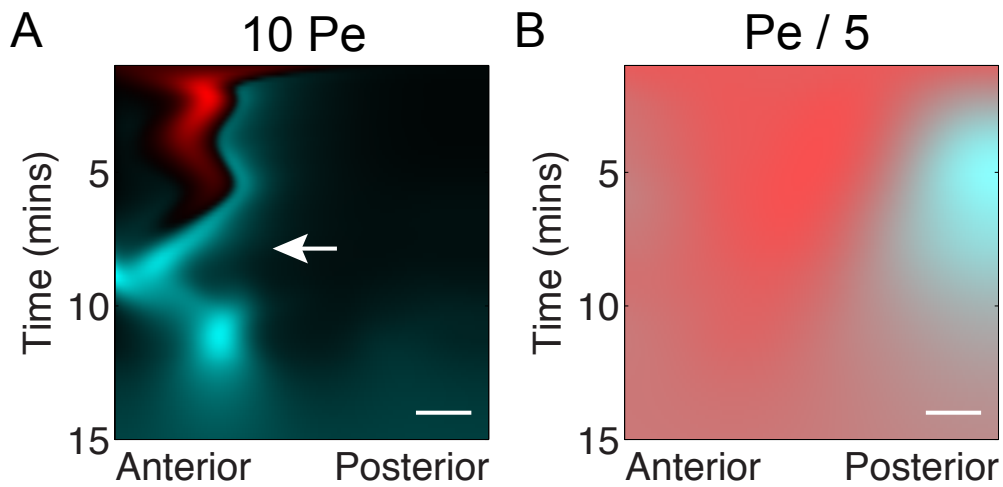


Figure S9. Sensitivity of the model to changes in the Péclet number. (A) Increasing Pe 10-fold by increasing flow velocities results in advection driving excessive anterior retraction of A and expansion of P , as well as much more pronounced enrichment of P at the leading edge of the domain (white arrow). Here, the degree of P domain expansion is ultimately sufficient to switch the system into the homogeneous posterior-like P steady state. (B) When Pe is reduced 5-fold by a decrease of flow velocities, anterior displacement of A is reduced. Here, posterior A -levels do not fall below a threshold required to allow formation of a P domain that is sufficiently large to persist once flows cease. Thus, the system reverts to the anterior-like steady state. Simulations were identical to Fig. 3A, but increasing or decreasing the magnitude of the velocity. Bars, 10 μm .

Table S1. Standard *C. elegans*-specific parameters

Parameter ^a	Species	
	<i>A</i> (PAR-6)	<i>P</i> (PAR-2)
L^b	134.6 μm	
ψ^b	0.174 μm^{-1}	
$\rho_{A/P}^c$	$\rho_A = \mathbf{1.56} \pm \mathbf{0.33} \mu\text{m}^{-3}$	$\rho_P = \mathbf{1.0} \mu\text{m}^{-3}$
D	0.28 $\mu\text{m}^2/\text{s}$	0.15 $\mu\text{m}^2/\text{s}$
k_{off}	5.4 $\times 10^{-3}/\text{s}$	7.3 $\times 10^{-3}/\text{s}$
k_{on}	8.58 $\pm \mathbf{1.7} \times 10^{-3} \mu\text{m}/\text{s}$	4.74 $\pm \mathbf{1.2} \times 10^{-2} \mu\text{m}/\text{s}$
$k_{\text{AP/PA}}$	$k_{\text{AP}} = 0.190 \mu\text{m}^2/\text{s}$	$k_{\text{PA}} = 2.0 \mu\text{m}^4/\text{s}$
α/β	$\alpha = 1$	$\beta = 2$

^a Measured values are shown in **bold** \pm **SD**. Unless otherwise specified, the values shown are used in all numerical analyses. D and k_{off} from (18).

^b For the model, we consider a prolate spheroid with radii $27 \times 15 \times 15 \mu\text{m}$. L is the perimeter along the long axis and ψ is the surface to volume ratio.

^c Densities are in dimensionless units of fluorescence per μm^3 , and normalized for convenience such that $\rho_P = 1 \mu\text{m}^{-3}$. Note that rescaling the measure of fluorescence amounts to a rescaling of $\rho_{A/P}$ and $k_{\text{AP/PA}}$, which becomes apparent if the governing equations are written in dimensionless form.

Table S2. Estimated protein concentrations^a

Protein	[Embryo] ^b	[Cytoplasm]	ρ_S ^c	Φ ^d
PAR-6	171 ± 23 nM	145 ± 22 nM	177 μm^{-2}	$7.2 \times 10^3 \mu\text{m}^{-2}$
PAR-2	79 ± 23 nM	41 ± 20 nM	266 μm^{-2}	$4.3 \times 10^3 \mu\text{m}^{-2}$

^a Mean ± SD shown.

^b Estimate of absolute cytoplasmic concentration that is attained if all molecules are in the cytoplasm.

^c Estimate of peak surface density.

^d The number of molecules per diffusion area, i.e. the membrane area explored by a single PAR molecule diffusing with coefficient D before dissociating ($\Phi \approx \rho_S l^2 \pi/4$, where $l = \sqrt{D/k_{\text{off}}}$).

Table S3. Strains used

Strain	Genotype	Source
JJ1473	unc-119(ed3) III; zuIs45[nmy-2::NMY-2::GFP+ unc-119(+)]	(34)
JJ1743	par-6(tm1425)/hIn1[unc-54(h1040)] I; him-8(e1489) IV.	CGC
VC1313	par-2(ok1723)/sC1[dpy-1(s2170)] III.	CGC ^a
TH25	unc-119(ed3) III; ddIs8 [pie-1::GFP::par-6(cDNA); unc-119(+)]	
TH120	unc-119(ed3) III; ddIs25; ddIs26[mCherry::T26E3.3 (par-6) + unc-119(+)]	(35)
TH129	unc-119(ed3) III; ddIs25[pie-1::GFP::par-2[RNAi res. SacI/MluI]] ^b + unc-119]	(35)
TH209	unc-119(ed3) III; ddIs31[pie-1::mCherry::par-2 + unc-119(+)]	(36)
TH411	unc-119(ed3) III; ddIs8; ddIs31	
TH412	unc-119(ed3) III; par-2(ok1723)/sC1[dpy-1(s2170)] III.	
TH413	unc-119(ed3) III; par-2(ok1723); ddIs25	
TH414	unc-119(ed3) III; par-2(ok1723); ddIs238[pie-1::GFP::par-2(CAI 0.26) + unc-119(+)]	
TH415	unc-119(ed3) III; par-2(ok1723); ddIs239[pie-1::GFP::par-2(CAI 0.6) + unc-119(+)]	
TH416	ddIs25; par-6(tm1425)/hIn1[unc-54(h1040)] I; him-8(e1489) IV. ^c	
TH417	ddIs8; par-2(ok1723)/sC1[dpy-1(s2170)] III. ^c	

^a Strain constructed by the *C. elegans* Gene Knockout Consortium and obtained via CGC.

^b RNAi resistance is provided by replacing the SacI/MluI fragment by a synthetic gene fragment codon optimized for mismatch with the endogenous sequence (fragment CAI = 0.41).

^c Presence of unc-119(ed3) unknown.

SOM Movie Legends

Movie S1. Transient segregation of aPAR by advection. Full time-course of simulation in Fig. 1A-B showing aPAR (red) and applied flow velocity $v(x, t)$ (dashed black line). Time (min:sec). Bars, 10 μm .

Movie S2. Transient segregation of PAR-6 in a *par-2* RNAi embryo. Full timecourse of Fig. 1C-D showing GFP::PAR-6 segregating with cortical flows in embryos depleted for PAR-2. PAR-6 returns to the posterior as flows attenuate. Time (min:sec). Bars, 10 μm .

Movie S3. Advection-triggered polarization in the full model. Full time-course of simulation in Fig. 3A, C showing aPAR (red), pPAR (cyan), and applied flow velocity, $v(x, t)$ (dashed black line). Time (min:sec). Bars, 10 μm .

Movie S4. Polarization of PAR-2 and PAR-6 in a wild-type embryos. GFP::PAR-6 (red) and mCherry::PAR-2 (cyan) are shown. Here, segregation of PAR-6 by flows allows formation of a posterior PAR-2 domain that prevents spread of anterior-enriched PAR-6 back into the posterior once flows cease. Time (min:sec). Bars, 10 μm .

References and Notes

1. A. Turing, *Philos Trans R Soc Lond, B, Biol Sci* **237**, 37 (1952).
2. J. Howard, S. W. Grill, J. S. Bois, *Nat Rev Mol Cell Biol* **12**, 400 (2011).
3. J. Bois, F. Jülicher, S. Grill, *Physical Review Letters* **106**, 029103 (2011).
4. B. Etemad-Moghadam, S. Guo, K. J. Kemphues, *Cell* **83**, 743 (1995).
5. L. Boyd, S. Guo, D. Levitan, D. T. Stinchcomb, K. J. Kemphues, *Development* **122**, 3075 (1996).
6. J. L. Watts, *et al.*, *Development* **122**, 3133 (1996).
7. J. Betschinger, K. Mechtler, J. A. Knoblich, *Nature* **422**, 326 (2003).
8. R. Benton, D. St Johnston, *Cell* **115**, 691 (2003).
9. G. Tanentzapf, U. Tepass, *Nat Cell Biol* **5**, 46 (2003).
10. E. Munro, J. Nance, J. R. Priess, *Dev Cell* **7**, 413 (2004).
11. A. D. Chalmers, *et al.*, *Development* **132**, 977 (2005).
12. Y. Hao, L. Boyd, G. Seydoux, *Dev Cell* **10**, 199 (2006).
13. C. Hoege, *et al.*, *Curr Biol* **20**, 1296 (2010).
14. M. Mayer, M. Depken, J. S. Bois, F. Jülicher, S. W. Grill, *Nature* **467**, 617 (2010).
15. C. R. Cowan, A. A. Hyman, *Nature* **431**, 92 (2004).
16. A. A. Cuenca, A. Schetter, D. Aceto, K. Kemphues, G. Seydoux, *Development* **130**, 1255 (2003).
17. S. N. Hird, J. G. White, *The Journal of Cell Biology* **121**, 1343 (1993).
18. N. W. Goehring, C. Hoege, S. W. Grill, A. A. Hyman, *The Journal of Cell Biology* **193**, 583 (2011).
19. A. Jilkine, A. F. M. Marée, L. Edelstein-Keshet, *Bull. Math. Biol.* **69**, 1943 (2007).
20. F. Tostevin, M. Howard, *Biophys J* **95**, 4512 (2008).
21. C. A. Shelton, J. C. Carter, G. C. Ellis, B. Bowerman, *The Journal of Cell Biology* **146**, 439 (1999).
22. M.-C. Tsai, J. Ahringer, *The Journal of Cell Biology* **179**, 397 (2007).
23. S. Zonies, F. Motegi, Y. Hao, G. Seydoux, *Development* **137**, 1669 (2010).
24. Y. Mori, A. Jilkine, L. Edelstein-Keshet, *Biophys J* **94**, 3684 (2008).
25. A. Gamba, *et al.*, *Proc Natl Acad Sci USA* **102**, 16927 (2005).
26. Y. Arai, *et al.*, *Proc Natl Acad Sci USA* **107**, 12399 (2010).
27. A. Jilkine, L. Edelstein-Keshet, *PLoS Comput Biol* **7**, e1001121 (2011).
28. S. Redemann, *et al.*, *Nat Methods* **8**, 250 (2011).
29. D. P. Hill, S. Strome, *Dev Biol* **125**, 75 (1988).
30. C. A. Shelton, B. Bowerman, *Development* **122**, 2043 (1996).
31. R. S. Kamath, J. Ahringer, *Methods* **30**, 313 (2003).
32. S. Redemann, *et al.*, *PLoS ONE* **5**, e12301 (2010).
33. C. DeRenzo, K. J. Reese, G. Seydoux, *Nature* **424**, 685 (2003).
34. J. Nance, E. M. Munro, J. R. Priess, *Development* **130**, 5339 (2003).
35. S. Schonegg, A. T. Constantinescu, C. Hoege, A. A. Hyman, *Proc Natl Acad Sci USA* **104**, 14976 (2007).
36. C. P. Brangwynne, *et al.*, *Science* **324**, 1729 (2009).